Available online at www.sciencedirect.com
SCIENCE DIRECT®
International Journal of Heat and Mass Transfer 49 (2006) 1529–1546
International Journal of HEAT and MASS TRANSFER
www.elsevier.com/locate/ijhmt

On the Rayleigh–Taylor instability for confined liquid films with injection through the bounding surfaces

F.F. Abdelall, S.I. Abdel-Khalik *, D.L. Sadowski, S. Shin, M. Yoda

G.W. Woodruff School of Mechanical Engineering, Georgia Institute of Technology, 771 Ferst Drive, Atlanta, GA 30332-0405, USA

Received 1 April 2005; received in revised form 15 July 2005
Available online 2 December 2005

Abstract

An experimental and numerical investigation has been conducted to evaluate the hydrodynamic characteristics of a thin liquid film bounded by a downward-facing flat wall through which the liquid is continually injected. Both horizontal and inclined surfaces have been examined. The effect of different parameters, namely, the film thickness, liquid injection velocity, inclination angle and liquid properties on liquid film behavior have been examined. Non-intrusive optical techniques have been used to follow the transient evolution of the film free surface. Specifically, the frequency of droplet detachment, the size of the detached droplets, and the penetration depth prior to droplet detachment have been measured. These data have been compared against predictions of a mechanistic numerical model based on the level contour reconstruction front tracking method. The numerical model predictions are in good agreement with the experimental data.

Keywords: Rayleigh–Taylor instability; Liquid film stability; Interface morphology; Numerical front tracking

1. Introduction

More than a century ago, Lord Rayleigh studied the stability of a density interface subject to a constant gravitational acceleration. Taylor extended Rayleigh's analysis to consider density interfaces subject to arbitrary accelerations. Here, we consider the case of Rayleigh–Taylor instability when a heavy immiscible fluid is situated above a light fluid under the influence of gravity. Under such conditions, the density interface becomes unstable for certain perturbation wavelengths; these perturbations evolve into bubbles of light fluid and spikes of heavy fluid that penetrate into the heavy and light fluids, respectively [1]. This phenomenon has been the subject of numerous experimental and numerical studies because of its fundamental importance in a variety of practical applications (see Ref. [2] for a recent summary of the literature).

Our interest in this problem derives from our work on first wall protection for inertial fusion reactors. Among the proposed wall protection schemes for such reactors is the "porous wetted wall" concept, originally proposed by Los Alamos in 1972 [3,4], and later adopted by several conceptual reactor designs [5–10]. In a typical rendition of such a design [5], a thin (0.4–0.6 mm) film of liquid lead is permitted to form on the inner surface of the reactor cavity by continually injecting the liquid lead through the porous silicon carbide first wall (Fig. 1). The X-rays and ions produced by the exploding targets at the center of the reactor cavity deposit their energy in the thin liquid lead film and the vapor cloud produced by lead evaporation, thereby protecting the underlying silicon carbide first wall. Recondensation of the vapor cloud allows the energy absorbed in the film to be recovered prior to the next target explosion, albeit over a longer time period, hence limiting first wall heating and thermal stress.

The hydrodynamics of the porous wetted wall protection scheme, as applied to the downward-facing upper surface of the inertial fusion reactor cavity (Fig. 1), can be

* Corresponding author. Tel.: +1 404 894 3719; fax: +1 404 894 8496.
E-mail address: said.abdelkhalik@me.gatech.edu (S.I. Abdel-Khalik).

0017-9310/$ - see front matter © 2005 Elsevier Ltd. All rights reserved.
doi:10.1016/j.ijheatmasstransfer.2005.07.055

Nomenclature

A	surface area, m^2
D	equivalent diameter, m
g	gravitational acceleration, m/s^2
h_0	liquid film mean thickness, m
I	indicator heaviside function
l	length scale, $(\sigma/[g(\rho_L - \rho_G)])^{1/2}$, m
n	unit vector normal to the interface
p	non-dimensional pressure
P_0	pressure scale, $\rho_L U_0^2$, N/m^2
Q	volume flow rate, m^3/s
Re	Reynolds number, $\rho_L l U_0/\mu_L$
T	temperature, K
t	non-dimensional time
t_0	time scale, l/U_0, s
u	non-dimensional fluid velocity vector
U_0	velocity scale, $(gl)^{1/2}$, m/s
u, v, w	fluid velocity components in Cartesian coordinates, m/s
We	Weber number, $\rho_L l U_0^2/\sigma$
x	non-dimensional position vector
x, y, z	Cartesian coordinates, m
z_0	initial liquid film thickness, m

Greek symbols

δ	Dirac delta function
ε_s	amplitude of initial perturbation, m
θ	inclination angle, degrees
κ	twice the mean interface curvature
μ	dynamic viscosity, $N\,s/m^2$
μ^*	dynamic viscosity ratio, μ_G/μ_L
ρ	density, kg/m^3
ρ^*	density ratio, ρ_G/ρ_L
σ	surface tension, N/m; standard deviation, s

Subscripts

f	quantity at interface
G	gas phase
L	liquid phase

Superscripts

*	property ratio or non-dimensional quantity
+	non-dimensional quantity

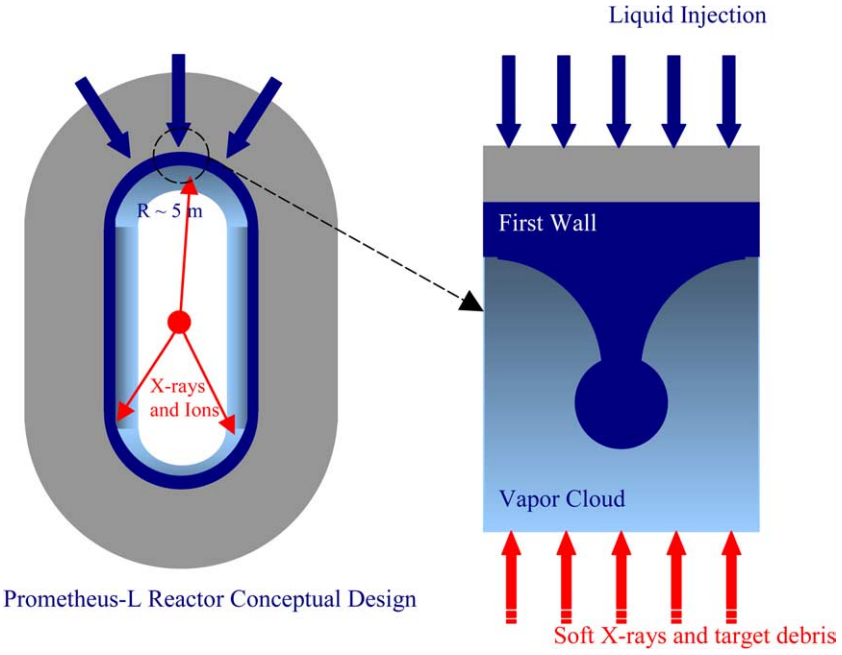

Fig. 1. Schematic illustration of the proposed thin liquid film protection scheme for the inertial fusion energy IFE system.

viewed as a variation of the Rayleigh–Taylor (henceforth RT) instability problem. Numerous experimental and theoretical studies of the RT instability have been reported in the literature; however, no work has heretofore been reported on the evolution and stability of thin liquid films on downward-facing surfaces with liquid injection through the wall. To this end, an experimental and numerical investigation has been conducted to examine the hydrodynamics of thin liquid films formed on horizontal and inclined downward-facing surfaces of a porous wall with continuous liquid injection normal to the surface. The objective is to determine the effect of different parameters, namely

liquid injection velocity, film thickness, inclination angle, and liquid properties, on liquid film behavior. Specifically, the effects of these parameters on the spatial and temporal evolution of the film free surface, i.e., the frequency of liquid droplet formation and subsequent detachment, the size of the detached droplets, and the time history of the penetration depth, are quantified. The experimental data are used to validate predictions of a numerical code based on a level contour reconstruction front tracking technique [11–14]. The numerical code is designed to perform three-dimensional simulations of multiphase flows with complete transport and interface physics, including a robust treatment of interface merging and breakup. Validation of this code will give system designers a powerful tool for identifying the requisite parameter ranges for successful operation of the thin liquid film protection scheme. Aside from its direct applicability to wetted-wall protection systems design, the experimental data in itself is valuable, inasmuch as it addresses a complex fluid dynamics problem, which has heretofore not been investigated, namely the bounded Rayleigh–Taylor instability with injection of the heavier fluid through the boundary.

2. Literature review

The interface between a dense fluid above a lighter fluid in a gravitational field pointing towards the lighter fluid is unstable to certain perturbation wavelengths. These perturbations evolve into bubbles of light fluid that mushroom into the heavy fluid, causing it to form spikes which penetrate into the lighter fluid. This Rayleigh–Taylor instability can be divided into three stages [15] as depicted in Fig. 2(a). In the case of a flowing film on a downward-facing inclined bounding surface, the flow, which starts at the top end of the bounding plate, is initially parallel to the surface. Fluid fluctuations at the liquid–gas interface then begin to develop in a wavy transition region; this intermediate stage is characterized by the formation of spikes and detachment of droplets as presented in Fig. 2(b).

This case is an "inverted" form of the problem of RT instability of a thin viscous liquid film above a wall, of importance in geophysical fluid dynamics, studied by Yiantsios and Higgins using an asymptotic non-linear analysis [16] and Newhouse and Pozrikidis [17], among others. Both studies focused on the effects of viscosity ratio and surface tension on the initial stages of droplet formation and penetration into the denser fluid, followed by a trailing plume.

Experiments on the RT instability were performed by, among others, Lewis [18], Duff et al. [19], and Popil and Curzon [20]. Lewis [18], who studied the RT instability created by imposing a pressure difference across a column of water, concluded that the instability could be divided into three stages: (1) an initial stage characterized by an exponential increase in the amplitude of the interfacial waves, (2) a transition stage that includes the formation of "mushrooms" of air that start to penetrate into the liquid, and (3) a final stage where spikes of air penetrate the liquid at a uniform velocity that scales with the square root of the gravitational acceleration. The initial stage appears to have significant variation in the growth rates of the wave amplitudes, even for experiments carried out with similar initial conditions (see Fig. 16 of [18]). Duff et al. [19] studied the RT instability for an argon–bromine gas mixture falling into air or helium, using a steel diaphragm to isolate the two gases before starting the experiment. They showed that

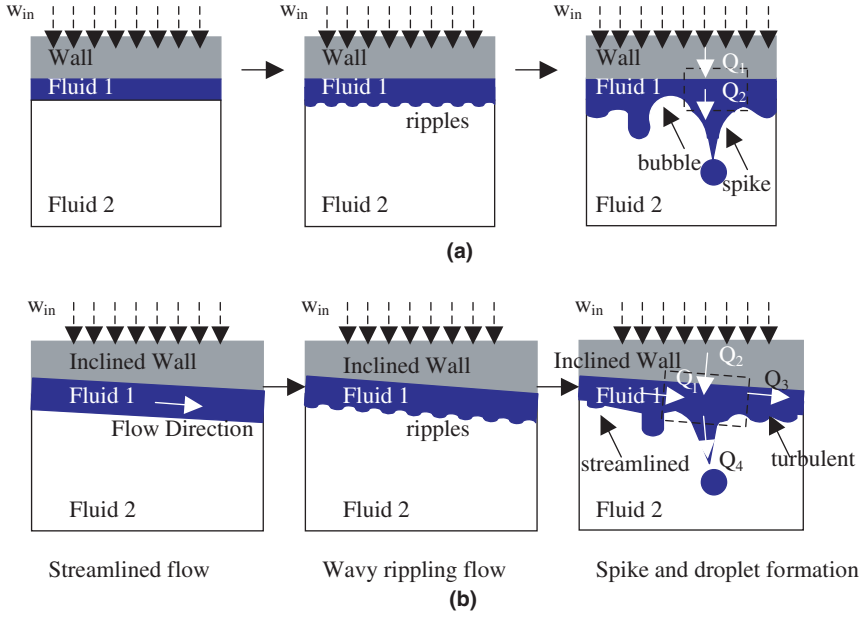

Fig. 2. Schematic illustration of the bounded Rayleigh–Taylor instability sequence with transpiration through the boundary: (a) horizontal boundary configuration and (b) inclined boundary configuration.

diffusion could be used to explain essentially all the features of the initial growth of the perturbations.

Popil and Curzon [20], who used an accelerated tank filled with water to study the RT instability, generating standing waves at the free surface using horizontal electrodes, demonstrated that the dynamics of the instability were reproducible for initial perturbations with a well-characterized amplitude and phase. The amplitude of the resultant spikes measured with respect to the initial water level was considerably larger than the initial amplitude before the acceleration. Lange et al. [21], who examined the temporal evolution of a water–sand (polydisperse glass spheres) interface driven by gravity, showed that the initial disturbances of the interface grow exponentially at the beginning of the pattern-forming process and that the growth rate increases with increasing wave number.

Numerous theoretical and numerical studies of the Rayleigh–Taylor instability have also been reported in the literature. The evolution of a single initial perturbation from small to large amplitude is now fairly well-studied for two-dimensional or axisymmetric flows. Most of these calculations have assumed inviscid flow or at least very small viscosities, neglected surface tension effects, and imposed a semi-infinite boundary for each fluid. Analytical and simple ordinary differential equations (ODE) solutions for perturbation growth during the first stage where linear theory is applicable have been well-established for some time. One means of analyzing the RT instability is to investigate only the long-scale phenomena via lubrication or long-wave theory [22,23]. Recently, volume of fluid (VOF) [24], front tracking [25], level set [26], and lattice Boltzmann [27] methods have also been used in two- and three-dimensional simulations of the RT instability.

Glimm et al. [25] modeled the RT instability for two-dimensional incompressible inviscid fluid flows using a front tracking technique. They carried out studies for statistically distributed heterogeneities in the initial perturbation and concluded that these heterogeneities can vary the flow characteristics. Tryggvason and Unverdi [28–30] solved the three-dimensional Navier–Stokes equations for weak stratification also using the front tracking method. They found that the amplitude increases with decreasing viscosity and thus leads to the formation of rolled-up vortices. Their results show a significant difference in the computed vortex structure for 2D and 3D simulations. For 2D simulations, the rolled-up vortex remains at the original interface whereas in 3D simulations it propagates away from the interface, thereby causing the disturbance to penetrate much faster. Li [31] used a level set approach to analyze 3D RT instability in compressible fluids. A second-order Total Variation Diminishing scheme with a fully parallelized algorithm was used to solve the 3D Euler equations. He compared his results for terminal velocity, which is proportional to the square root of gravitational acceleration and bubble radius, with those of Taylor [32] and suggested that transition from constant velocity to constant acceleration was caused by bubble merger. Lattice Boltzmann simulations have also been used to study the RT instability in 3D [33].

3. Numerical model

A numerical model based on the level contour reconstruction method has been developed to analyze the problem of a bounded horizontal thin liquid film Rayleigh–Taylor instability with injection through the boundary [11–14]. This technique stems from Tryggvason's front tracking method for isothermal multifluid flows [28–30]. An important advantage of this method is its ability to automatically and naturally handle interface merging and breakup in three-dimensional flows. The elements are meshed on a level contour of an indicator function. This characteristic indicator function is a Heaviside function which takes the value of unity in one fluid and zero in the other fluid. The operations of element addition, deletion and reconnection are carried out simultaneously in one step and without resorting to bookkeeping or element connectivity.

One set of transport equations valid for both fluids is used. Delta-function source terms, which act only at the interface, are used in the local single field formulation in order to incorporate the effect of the interface. An indicator Heaviside function is employed to define the material property fields for the entire domain. A single non-dimensional momentum equation is written for the entire flow field and the forces due to surface tension are accounted for at the interface as body forces, which act only at the interface. Instead of an infinitely-thin interface, the front is represented by a finite thickness, by distributing the interfacial source terms over several grid points near the interface, thereby providing numerical stability and smoothness. Numerical diffusion is not present since this thickness remains constant for all time. In non-dimensionalizing the governing equations and boundary conditions, the following scales are used: the length scale $l = (\sigma/[g(\rho_L - \rho_G)])^{1/2}$, the velocity scale $U_0 = (gl)^{1/2}$, the pressure scale $P_0 = \rho_L U_0^2$, and the time scale $t_0 = l/U_0$.

The non-dimensional momentum equation in conservative form can be expressed as

$$\frac{\partial \rho^+ \mathbf{u}}{\partial t} + \nabla \cdot (\rho^+ \mathbf{u}\mathbf{u}) = -\nabla p + \rho^+ \mathbf{g} + \frac{1}{Re}\nabla \cdot \mu^+ (\nabla \mathbf{u} + \nabla \mathbf{u}^T) + \int_A \frac{1}{We}\kappa \mathbf{n}\delta(\mathbf{x} - \mathbf{x}_f)\,dA \quad (1)$$

where

$$\frac{\rho_G}{\rho_L} = \rho^*, \quad \frac{\mu_G}{\mu_L} = \mu^* \quad (2)$$

$$\rho^+ \equiv \frac{\rho(\mathbf{x},t)}{\rho_L} = 1 + (\rho^* - 1)I(\mathbf{x},t) \quad (3)$$

$$\mu^+ \equiv \frac{\mu(\mathbf{x},t)}{\mu_L} = 1 + (\mu^* - 1)I(\mathbf{x},t) \quad (4)$$

$$Re = \frac{\rho_L U_0 l}{\mu_L}, \quad We = \frac{\rho_L U_0^2 l}{\sigma} = \frac{\rho_L}{\rho_L - \rho_G} \quad (5)$$

Table 1
Values of the scaling length, velocity, and time, along with the Reynolds number for various working fluids [34–36]

	Water, H_2O		20% Glycerol		Lead, Pb		Flibe, $LiF–BeF_2$		
T (K)	293	323	293	323	700	800	773	873	973
l (mm)	2.73	2.65	2.62	2.56	2.14	2.12	3.35	3.22	3.17
U_0 (mm/s)	163.5	161.2	160.5	158.6	144.7	144.2	181.4	177.8	176.4
t_0 (ms)	16.7	16.4	16.4	16.2	14.8	14.7	18.5	18.1	18
Re	445	771.2	250	777.8	1618	1831	81.8	130.8	195.3

In this formulation, p is the pressure, $\mathbf{g}$ is the gravitational acceleration, σ is the surface tension, and κ is twice the mean interface curvature.

Values of the length, velocity, and time scales, along with the Reynolds number for candidate wall-protection fluids for inertial fusion reactors, along with the two test fluids used in this investigation, are given in Table 1. The selected length scale results in a Bond number value of unity ($Bo = g(\rho_L - \rho_G)l^2/\sigma$), while the selected velocity scale causes the Weber number to be a function of only the density ratio, ρ^*; it approaches unity as ρ^* approaches zero. It should be noted that the Atwood number ($A = (\rho_L - \rho_G)/(\rho_L + \rho_G)$) also approaches unity as ρ^* approaches zero. Numerical simulations were carried out using the long wave length initial surface perturbations (mode number 1). A fine mesh ($100 \times 100 \times 100$) was used; the adequacy of the mesh size has been confirmed through calculations with coarser grids. Computational resources prevented the use of finer mesh resolution. For mode number one, the perturbation wavelength is equal to the calculation box size in the x

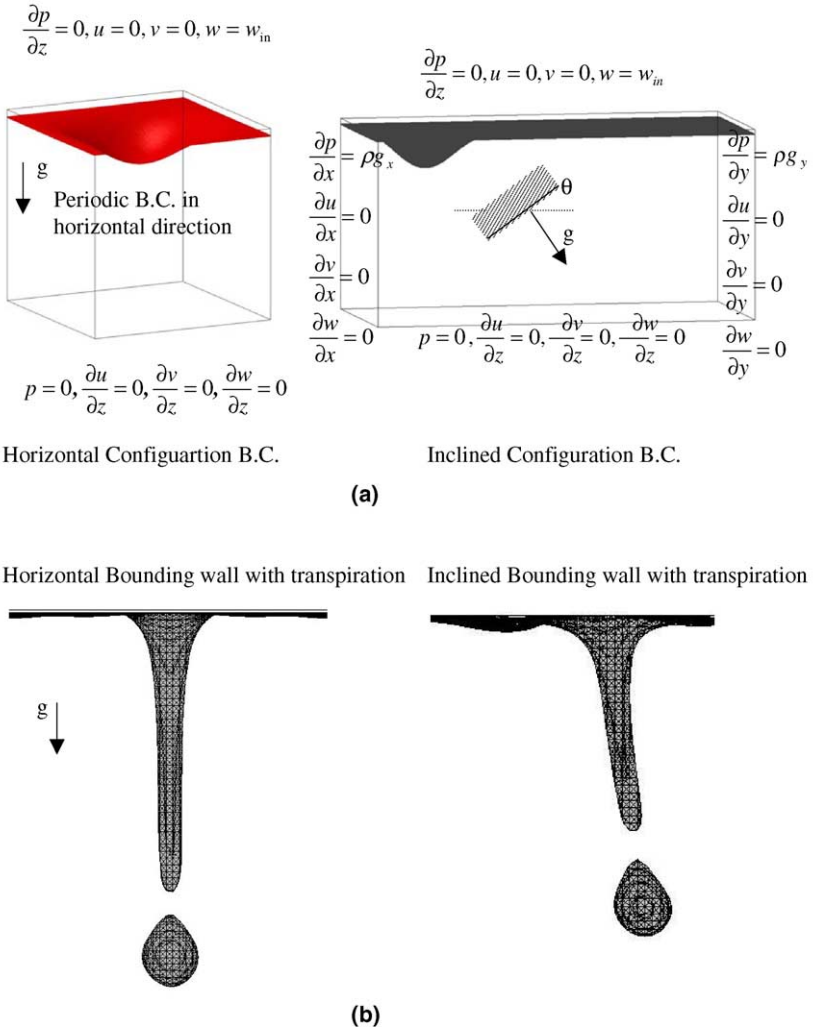

Fig. 3. Configuration of the grid elements for the bounded Rayleigh–Taylor instability numerical simulation utilized in modeling horizontal and inclined bounding surfaces with liquid injection through the wall surface: (a) initial surface configuration and boundary conditions and (b) detachment point.

(L_x) and y (L_y) directions. The initial liquid–gas interface is defined using the following formulation:

$$z_s = z_0 - \frac{\varepsilon_s}{4}\left(\cos\left(\frac{2\pi(x_s - L_x/2)}{L_x}\right) + 1\right) \times \left(\cos\left(\frac{2\pi(y_s - L_y/2)}{L_y}\right) + 1\right) \quad (6)$$

The calculation geometry and boundary conditions used to model horizontal and inclined downward-facing surfaces with liquid injection through the wall surface are depicted in Fig. 3(a). This corresponds to the uppermost point and adjacent sectors in the reactor cavity inner surface (Fig. 1). Liquid is injected at a specified normal velocity at the downward-facing top solid boundary, while an open boundary condition is used at the bottom surface. The use of a Neumann pressure boundary condition at the wall is reasonable since the film is relatively thin; the pressure distribution within the porous wall is not a part of this analysis. In the inclined configuration, rather than using periodic boundary conditions in the horizontal directions, Neumann conditions for velocity and hydrostatic pressure gradients are applied along the x- and y-directions. Eq. (6) was used to define the initial interface geometry for both horizontal and inclined films; gravitational and shear effects will likely distort the initial interface geometry for inclined plates. The evolution of the free surface from the initially perturbed interface to the fully developed spikes penetrating through the lighter fluid and necking to form droplets that detach at the pinch-off point was calculated for various combinations of the governing non-dimensional parameters. The growth patterns and the sequences are processed and analyzed to calculate several field parameters, including: the frequency of liquid droplet detachment, the volume and size of detached droplets, and the penetration depth for the developing spikes.

The detached droplet was isolated in order to determine the liquid volume enclosed by the constructed surface. This computed numerical volume is utilized in obtaining an equivalent droplet diameter based on the definition of the standard sphere volume ($D_{\text{equivalent}} = \sqrt[3]{(6\text{Volume}_{\text{numerical}})/\pi}$). In order to trace the time history of the penetration depth, the maximum vertical distance from the plate surface to the lowermost tip point of the developing spike or the detached droplet is stored in a temporal array. Fig. 3(b) depicts typical triangular grid elements utilized in the numerical simulation at the droplet detachment point for both horizontal and inclined bounding surfaces. A first-order, forward Euler integration in time was used. For the spatial discretization, the well-known staggered mesh scheme was used; all spatial derivatives except the convective term were approximated by standard second-order centered differences. The convective term in the momentum equation was discretized using second-order ENO procedure. Additional details regarding the level contour reconstruction model and the numerical solution scheme can be found in [11–14].

4. Experimental investigation

A recirculating experimental test facility has been constructed to study the hydrodynamics of thin liquid films injected through downward-facing porous walls (Fig. 4). The flow is started by forcing the working fluid through flexible tubing up from a reservoir into a constant-head supply tank using a sump pump placed in the reservoir. The fluid from the constant-head tank is allowed to flow through a porous Type-316L stainless steel rectangular plate which serves as the test section. The constant-head tank is placed at different heights above the test section to obtain a range of inlet pressures and hence liquid injection velocities. The injected liquid forms a thin film on the underside of the porous plate; the film then grows downwards and forms spikes that "neck" and detach as droplets, which fall into the light fluid (ambient air). The liquid droplets ultimately fall into the reservoir, from which the liquid is recirculated back into the constant-head tank. A list of the various components used in the experimental test facility is given in Fig. 4.

The test section is a porous Type 316L stainless steel rectangular plate (thickness 1.6 mm) fed by a stainless steel plenum, capped by a 12.7 mm thick polycarbonate sheet. The porous plate dimensions (about 12×18 cm) are considerably larger than the characteristic length scale of the flow (see Table 1) and are, therefore, expected to adequately model the behavior of the much larger surfaces in a wetted reactor wall (radius ~5 m); baffles under the plenum cap provide uniform pressure distribution over the inner surface of the porous plate in order to enhance uniformity of liquid injection. A rectangular cutout in the stainless steel plenum holds the plate, which is attached to the plenum with an epoxy adhesive (Hysol, LOCTITE E-120HP 29353). The test liquid supply line from the constant-head tank is connected to the stainless steel plenum through an intermediate shutoff valve.

4.1. Experimental procedure and design parameters

A range of liquid injection velocities through the porous plate were obtained by varying the constant-head tank levels leading to different inlet pressures, and thus flow rates. For a given constant-head tank level and porous plate "grade" (i.e., porosity), the average injection velocity through the plate was determined by collecting the injected fluid during a specified period of time; liquid injection velocities of $0.9–2.1 \times 10^{-3}$ m/s were used in these experiments. The maximum expanded uncertainty in the mass flow rate calculation for the conducted experimental runs in this investigation using a minimum time increment of 5 s as a limiting value is 5×10^{-5} kg/s which translates to an expanded uncertainty of 0.18×10^{-5} m/s in the velocity. The expanded uncertainty is twice the standard uncertainty and corresponds to a 95% confidence limit; additional details on the method used to estimate the uncertainty values for different parameters may be found in [13]. The test

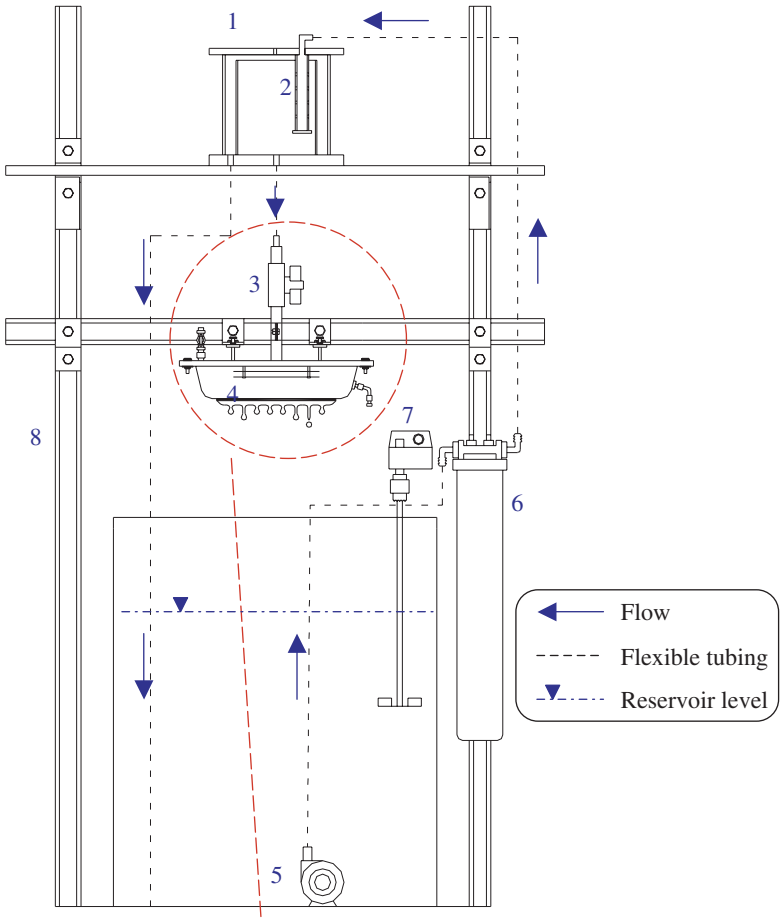

Number	Hardware Components
1	Constant-head supply tank
2	Perforated tube
3	Shutoff valve
4	Test section porous plate
5	Sump pump
6	Sub-micron filter
7	Fast stirrer
8	Unistrut frame
9	Air relief valve
10	Baffles
11	Porous plate plenum
12	Draining valve

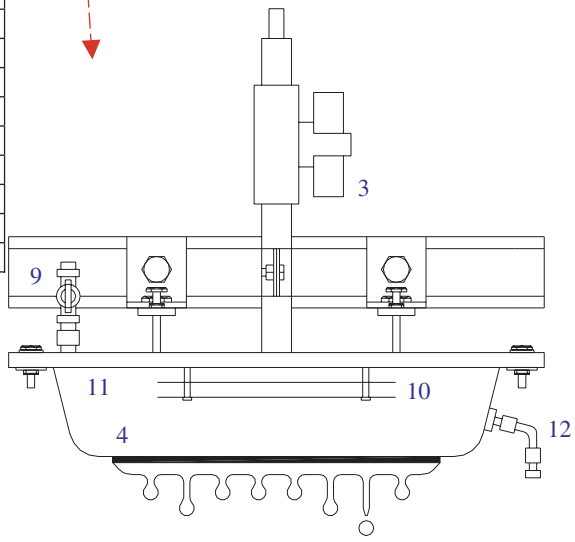

Fig. 4. Experimental setup (top) and close-up of test section (bottom).

facility is designed to reach higher injection velocities; however, at injection velocities exceeding 2.1×10^{-3} m/s, the developed liquid film forms continuous columns that do not neck or detach as droplets. On the lower end of the injection velocity range ($w_{in} \ll 0.9 \times 10^{-3}$ m/s), a discontinuous liquid film develops and droplets are separated by dry

spots. An alternative approach to independently vary the liquid film thickness and injection velocities was carried out by utilizing plates with different porosities (solid volume percentage range of 80–55%).

Water, glycerol and mixtures of the two are used as working fluids to provide a wide range of parameters to enable comparison between the experiments and the numerical model over the parameter ranges of interest. A glycerol–water solution was prepared from the pure fluids so that their compositions by weight were accurately known. In order to provide a Reynolds number value which is approximately half of that for pure water, a concentration of 20% glycerol was used in the aqueous solution (Table 1). The working fluids were selected such that the Reynolds numbers for water and 20% glycerol at room temperature ($T \approx 293$ K) fall within the range of interest for inertial fusion reactor coolants (see Table 1). The density, viscosity, and surface tension of the test fluids are 998.2 kg/m^3, 1×10^{-3} Ns/m^2, 7.28×10^{-2} N/m for water, and 1046.9 kg/m^3, 1.77×10^{-3} Ns/m^2, 7.09×10^{-2} N/m for 20% Glycerol solution at 293 K, respectively.

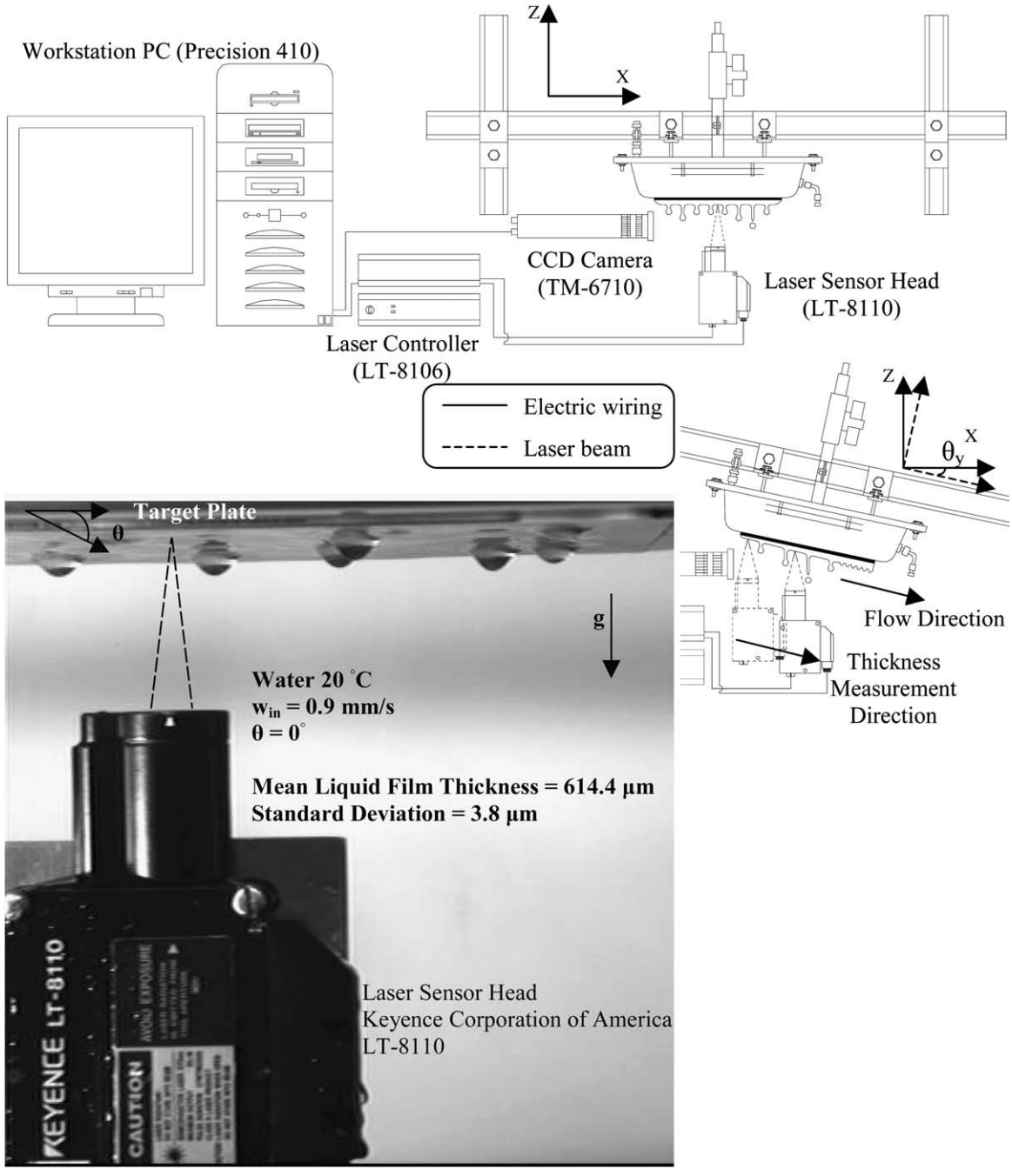

Fig. 5. Experimental instrumentation and data acquisition system for the horizontal and inclined boundaries and close-up of the non-intrusive measurement technique for the unperturbed liquid film thickness.

Inclination angles of 0° and 2.5° were utilized to investigate the effect of shear stress and liquid film drift on film behavior and droplet detachment. In order to accurately tilt the test section to the required angle of inclination θ_y, an electronic level was employed to measure the inclination angle directly on the plate. The angle measurement resolution is 0.1°. An inclination angle of 2.5° emerged as a limiting condition since higher angles of inclination produced high liquid film velocities on the downward-facing surface which caused droplet detachment to initiate beyond the porous plate length. In this inclined boundary setup, the thickness of the advected liquid film increases along the length of the plate from the uppermost point to the lowermost edge. The flow at the top edge of the inclined boundary is streamlined and impending droplets drift in the inclination direction. The fluid film drifting towards the lower edge of the bounding plate eventually becomes dominated by chaotic mixing, competing bubbles, impacting droplets, and random movement of relatively large parcels of fluid.

4.2. Instrumentation and data acquisition system

Precise measurement of the thickness of the "unperturbed" liquid film is necessary for accurate comparison with the numerical model predictions. The term "unperturbed" refers to the liquid film thickness away from spikes or droplets, which remains nearly constant for a given fluid and injection velocity. In order to monitor and measure the liquid film thickness, a non-intrusive technique based on a laser displacement measurement was employed using a system manufactured by Keyence (LT-8110). In this non-contact laser measurement, a 20 μW laser beam at 670 nm is focused on the target liquid film surface through a lens that is vibrated by a tuning fork. To measure the nominal ("unperturbed") film thickness, the laser beam is focused on a smooth spot on the film free surface (i.e., away from spikes or droplets preventing possible beam refraction) near the center of the horizontal rectangular porous plate. The reflected laser beam is reflected back into the sensor and redirected by means of half-mirrors to converge precisely on a pinhole over a light-receiving element. A detection signal is generated when the lens is precisely positioned for maximum light reception. The sensor detects the tuning fork's position when the laser beam focuses on the target film surface. The distance to the liquid film surface is then calculated. The measurement resolution is 0.2 μm.

The measurements of the liquid film thickness were preceded by a calibration step where the laser beam was focused on the dry plate surface to provide an absolute position reference. The instrumentation and data acquisition system for the horizontal and inclined boundary configurations as well as a close-up of the non-intrusive liquid film thickness measurement are depicted in Fig. 5. For every test run with a horizontal surface, 100 consecutive equally spaced measurements were taken over 10 s near the center of the porous plate. In order to accurately characterize and measure the spatial and temporal variations of the liquid film thickness in the inclined configuration, measurements were made at four equally-spaced locations along the centerline of the bounding rectangular plate in the flow direction. The first measurement was taken 20 mm from the top edge of the plate; the next three measurements were made 10 mm away from the previous measurement location. Positioning and alignment of the laser sensor head were carried out using a four degree-of-freedom positioning system mounted on the test facility frame. At each of the four selected positions, 100 consecutive liquid film thickness measurements were obtained at 10 Hz.

Droplet formation and detachment were imaged using a progressive scan monochrome CCD camera (Pulnix TM-6710) at 120 Hz with an exposure time of 8.33 ms as 648×484 pixel images. The images were digitized onto a PC using a framegrabber card (Road Runner Camera Link board R3-PCI-CL-23-L, BitFlow Inc.). Standard grayscale gradient-based edge detection schemes were used to determine the edge of the droplets in each image. The droplet detachment time was measured by tracking the sequential evolutions of the contoured edges to the pinch-off point. The detaching droplets are approximated by prolate spheroids with major and minor axes a and b, respectively; these axis dimensions were obtained from the droplet edges. The equivalent droplet diameter $D_{\text{equivalent}}$ for the prolate spheroid was then calculated: $D_{\text{equivalent}} = (ab^2)^{1/3}$.

5. Results and discussion

In this section the experimental results are presented and compared with the corresponding predictions of the numerical model. The data include: liquid film thickness, liquid droplet detachment time, equivalent diameter for detached droplets, and penetration depth. The experimental runs were conducted using water and 20% glycerol as the working fluids. Each experimental run with a combination of test fluid, injection velocity, and inclination angle is given a specific letter-number designation. For example, for run number W090, the "W" refers to the fluid (water), "09" refers to $w_{\text{in}} = 0.9 \times 10^{-3}$ m/s, and the trailing "0" refers to the inclination angle ($\theta = 0°$). The runs were conducted for injection velocities of 0.9, 1.4, 1.7, 1.9 and 2.1 mm/s using water (W) and 20% glycerol (G) for both horizontal and inclined surfaces ($\theta = 2.5°$).

5.1. Liquid film thickness

Typical sequences of 100 measurements of the "unperturbed" liquid film thickness for a horizontal surface with water injection are shown in Fig. 6 (runs #W090 and W210 with $w_{\text{in}} = 0.9$ and 2.1 mm/s, respectively). These data are used to calculate the mean value (h_0) of and standard deviation (σ) in the unperturbed liquid film thickness (cf. Table 2). The Figure suggests the existence of a periodic variation in the film thickness. These "waves", with amplitudes of 1–2% of the mean film thickness and frequencies

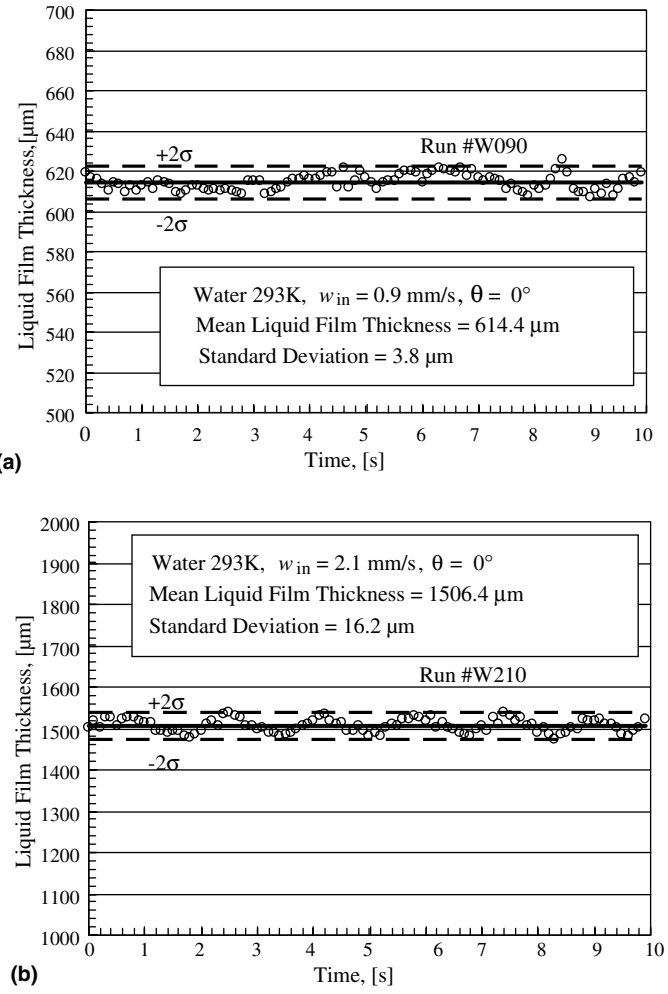

Fig. 6. Experimental data of the transient variation of the unperturbed liquid film thickness for horizontal boundaries ($\theta = 0°$): (a) run #W090 ($w_{in} = 0.9$ mm/s) and (b) run #W210 ($w_{in} = 2.1$ mm/s).

well below 1 Hz (droplet detachment frequencies appear to be ~2–3 Hz), could indicate the initial stages of droplet formation and reflect the most unstable perturbations for the liquid free-surface. Given their extremely low frequencies, however, we suspect that these waves reflect structural vibrations in the apparatus.

For a given porous plate "grade", the unperturbed liquid film thickness increases as the injection velocity increases; for example, the mean liquid film thickness increases by nearly 28% and 145% when the injection velocity of water increases from 0.9 to 1.7 mm/s and 2.1 mm/s, respectively. Using 20% glycerol instead of water requires a higher supply header pressure head and results in an increase in the measured liquid film thickness for the same injection velocity. The difference between the mean film thickness values for the two fluids becomes significant at higher injection velocities; differences of 12% and 28% were measured at injection velocities of 0.9 and 1.7 mm/s, respectively (Table 2).

For the inclined surface configuration, the thickness of the advected liquid film increases along the flow direction from the upper to the lower edge of the plate due to continuous liquid injection and delayed droplet formation. The fluctuations in liquid film thickness in the inclined configuration were measured at four equally-spaced locations along the centerline of the porous plate. Table 2 lists the mean and standard deviation values for the liquid film thickness obtained for each inclined surface test run for the four measured locations. Increasing the injection velocity or using 20% glycerol instead of water as the working fluid causes the mean liquid film thickness value to increase at the same axial location. Plots of the reduced mean film thickness as a function of the dimensionless injection velocity are shown in Fig. 7; the variables were scaled using the parameters given in Table 1.

5.2. Liquid droplet formation and detachment time

Results for the droplet detachment time from horizontal and inclined bounding surfaces with several injection velocities using water and 20% glycerol as working fluids are given in this section. These data represent the distribution of measured values for 100 different droplets; the mean droplet detachment time and the standard deviation among the experimental measurements are provided. The distribution of droplet detachment times is a direct result of the random nature of surface perturbations present during the experiments. It should be noted that in the hostile envi-

Table 2
Experimental mean and standard deviation (σ) values of the unperturbed liquid film thickness (h_0) for the experimental runs conducted using horizontal ($\theta = 0°$) and inclined ($\theta = 2.5°$) surfaces at several axial positions (x) along the flow direction for the inclined film

Runs	$\theta = 0°$		$\theta = 2.5°$							
			$x_1 = 20$ mm		$x_2 = 30$ mm		$x_3 = 40$ mm		$x_4 = 50$ mm	
	h_0 (μm)	σ (μm)	h_0 (μm)	σ (μm)	h_0 (μm)	σ (μm)	h_0 (μm)	σ (μm)	h_0 (μm)	σ (μm)
W09	614.4	3.8	217.8	21.4	324.2	21.2	419.2	12.8	812.4	16.8
G09	686.2	32.4	268.4	8.4	350.4	26.2	500.8	14.8	924.8	21.0
W14	713.0	13.8	293.4	6.2	441.2	4.4	622.0	26.6	917.2	59.4
W17	787.8	63.2	316.8	9.4	491.2	2.8	757.8	53.2	986.0	26.4
G17	1009.2	23.4	400.4	65.2	520.8	57.2	826.2	41.6	1267.8	31.8
W19	1131.8	105.4	399.2	8.2	597.2	54.8	930.4	62.4	1251.4	147.8
W21	1506.4	16.2	456.0	31.2	705.6	29.4	1168.6	41.4	1533.8	17.4

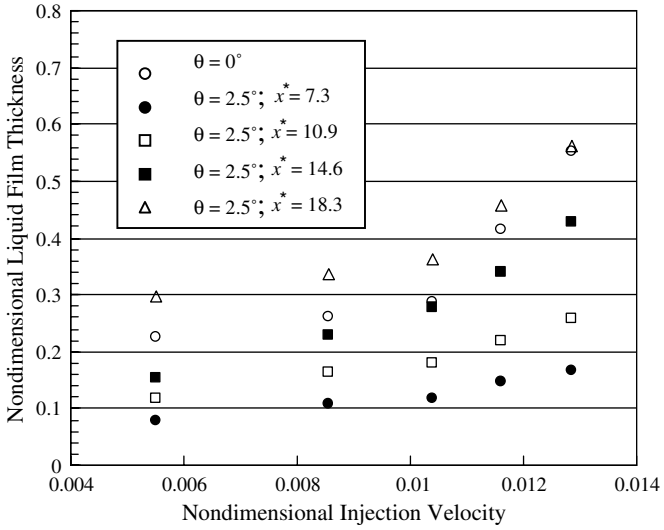

Fig. 7. Experimental data of the non-dimensional liquid film thickness varying with the non-dimensional injection velocity for $Re = 445$ using horizontal ($\theta = 0°$) and inclined ($\theta = 2.5°$) boundaries at several axial x^* positions.

ronment following target explosion in inertial fusion reactor cavities, the morphology of the initial film surface is expected to vary greatly. Thus, the sensitivity of the numerical results to the normalized initial perturbation amplitude ε_s/z_0 is tested by running the numerical model for a range of values, namely: $\varepsilon_s/z_0 = 0.1$, 0.25, 0.5, 0.75 and 1 (corresponding to an initial perturbation amplitude ranging from 10% to 100% of the unperturbed mean film thickness). The initial liquid film thickness z_0 used in the numerical analysis is assumed to be equal to the experimental value of the unperturbed mean film thickness h_0 (Table 2).

In the horizontal surface experiments, the droplet detachment time was measured by tracking the sequential evolutions of the developing spikes for 100 different droplets. Table 3 lists the experimental mean (t_d) and standard deviation (σ) of the detachment time, along with the numerically-predicted values. The numerical and experimental evolution sequences for run W090 are provided in Fig. 8(a). The numerical and experimental images are compared at the detachment or "pinch-off" point. Plots of the reduced mean detachment time as a function of the dimensionless injection velocity are shown in Fig. 9(a); the variables were scaled using the parameters given in Table 1.

The results in Table 3 show that the numerical model predictions of droplet detachment times over the examined range of perturbation amplitudes are essentially within two standard deviations (2σ) of the experimentally measured mean droplet detachment times. For lower injection velocities (e.g., run #W090) with a relatively thin unperturbed film thicknesses, the numerical and experimental results closely agree at lower normalized initial perturbation

Table 3
Experimental mean, standard deviation (σ) and numerical prediction values of the detachment time (t_d), equivalent droplet diameter (D) and maximum penetration depth (d) for the experimental and numerical runs conducted using horizontal bounding surfaces

Runs	Experiment		Normalized initial perturbation amplitude, ε_s/z_0				
			0.1	0.25	0.5	0.75	1
	t_d (s)	σ (s)	*Numerical predictions t_d (s)*				
W090	0.4652	0.0148	0.4992	0.4222	0.3634	0.3277	0.3042
G090	0.6724	0.0113	0.6784	0.5592	0.472	0.4234	0.3904
W140	0.4071	0.0091	0.4717	0.3999	0.3449	0.3124	0.2912
W170	0.3576	0.0085	0.4552	0.3872	0.3342	0.3037	0.2824
G170	0.5069	0.0105	0.5470	0.4564	0.3872	0.3531	0.3364
W190	0.3119	0.0106	0.4067	0.3442	0.2977	0.2732	0.2582
W210	0.2412	0.0140	0.3714	0.3179	0.2807	0.2604	0.2484
	D (mm)	σ (mm)	*Numerical predictions D (mm)*				
W090	8.2	0.2	8.6	8.5	8.6	8.7	8.7
G090	9.0	0.2	8.9	9.0	9.2	9.3	9.4
W140	8.6	0.1	8.8	8.8	8.8	8.9	9.0
W170	8.9	0.1	9.0	8.9	9.0	9.0	9.1
G170	9.9	0.2	9.5	9.5	9.6	9.9	10.2
W190	9.3	0.1	9.2	9.3	9.3	9.4	9.5
W210	9.6	0.2	9.6	9.7	9.8	9.9	10.0
	d (mm)	σ (mm)	*Numerical predictions d (mm)*				
W090	51.3	2.7	51.7	51.6	53.7	54.6	56.9
G090	74.4	1.9	73.1	74.4	78.4	83.1	87.9
W140	62.3	1.4	59.4	58.5	59.7	60.9	63.5
W170	69.8	1.8	63.5	63.0	63.8	65.4	67.4
G170	86.3	2.6	89.7	91.1	94.6	102.4	114.0
W190	76.7	2.5	73.1	72.1	74.5	78.5	82.9
W210	87.9	3.4	84.4	85.1	89.2	94.0	100.0

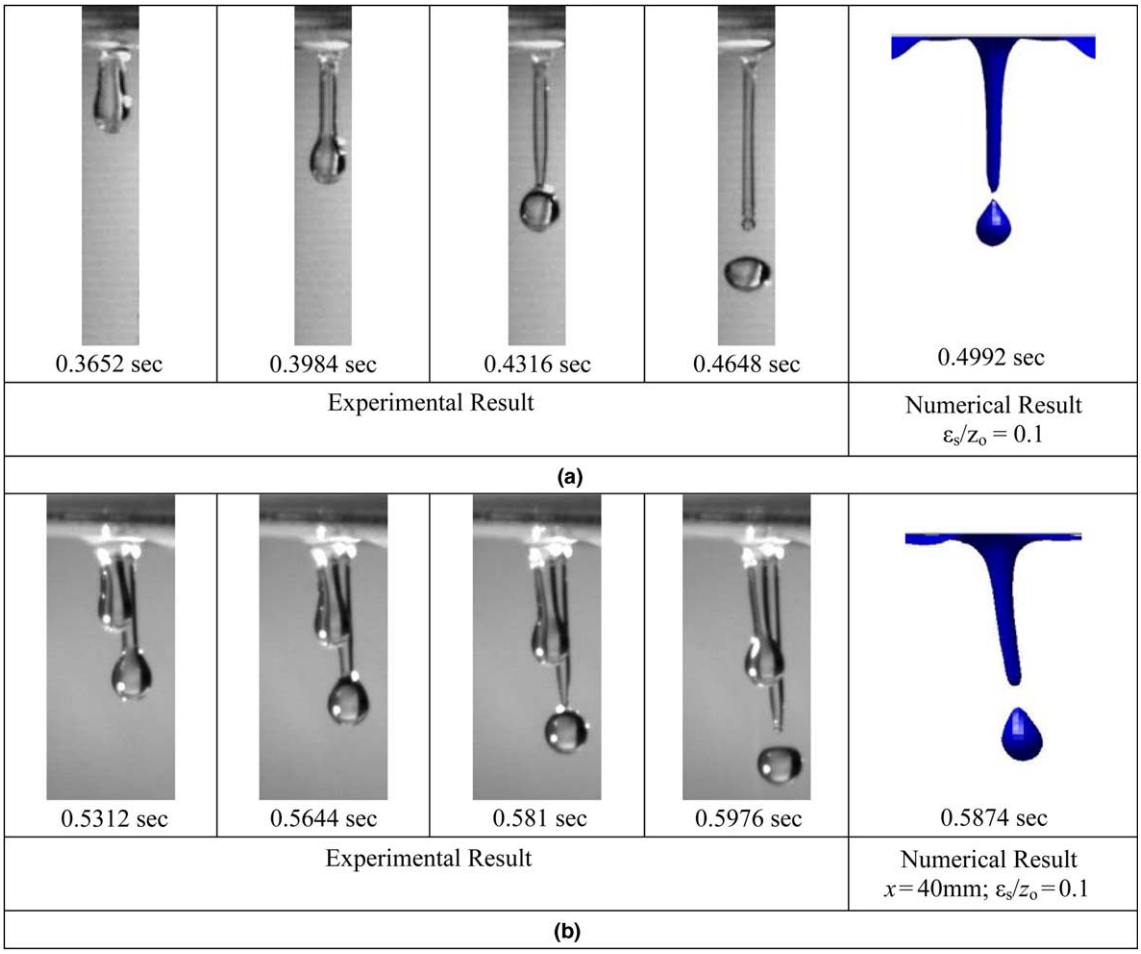

Fig. 8. Numerical and experimental liquid film evolution and droplet detachment sequence: (a) run W090 ($w_{in} = 0.9$ mm/s, $\theta = 0°$) and (b) run W0925 ($w_{in} = 0.9$ mm/s, $\theta = 2.5°$).

amplitudes ($\varepsilon_s/z_0 = 0.1$–0.25). On the other hand, for higher injection velocities (e.g., run #W210) with relatively thick unperturbed film thicknesses, good agreement between the numerical and experimental results is obtained at higher normalized initial perturbation amplitudes ($\varepsilon_s/z_0 \to 1$). This may be caused by the fact that in thick liquid films, spikes form and droplets detach from the preceding pinched-off spike thereby creating relatively large disturbance amplitudes, while in thinner liquid films surface leveling transpires after droplets detachment. Hence, close agreement between the numerical and experimental results is observed at higher normalized initial perturbation amplitude values ε_s/z_0 for thick liquid films (i.e., higher w_{in}) and at lower values of ε_s/z_0 for thin films (i.e., lower w_{in}).

For the inclined plate geometry, while the thickness increases along the flow direction, the numerical modeling was carried out using a constant initial liquid film thickness along the flow direction; calculations corresponding to each of the four measured thickness values along the plate were performed. The gravity-driven film on the inclined plate will, unlike the horizontal case, have a non-zero velocity component, and hence, an interfacial shear stress parallel to the wall. Droplet formation is delayed for the inclined plate configuration as compared to the horizontal surface setup due to liquid film drift, along with the tangential acceleration and associated shear stress. Based on the results provided in Tables 4 and 5, the measured mean droplet detachment time increased by ~30% and 20% when the surface is inclined ($\theta = 2.5°$) as compared to the horizontal setup for water and 20% glycerol, respectively (runs #W0925 and G0925). The numerical and experimental evolution sequences for run W0925 are shown in Fig. 8(b); the images correspond to the detachment or pinch-off point. Droplets detaching from the inclined surfaces were captured near the upper edge away from the somewhat chaotic region near the lower end of the inclined plate. The experimental results for variation of the non-dimensional detachment time with the non-dimensional injection velocity, along with the corresponding numerical results carried out for different axial positions and initial perturbation amplitudes, are presented in Fig. 9(b).

The numerical results indicate that for thinner liquid films, an increase in the detachment time is expected. For instance, for run #W2125 with a normalized initial pertur-

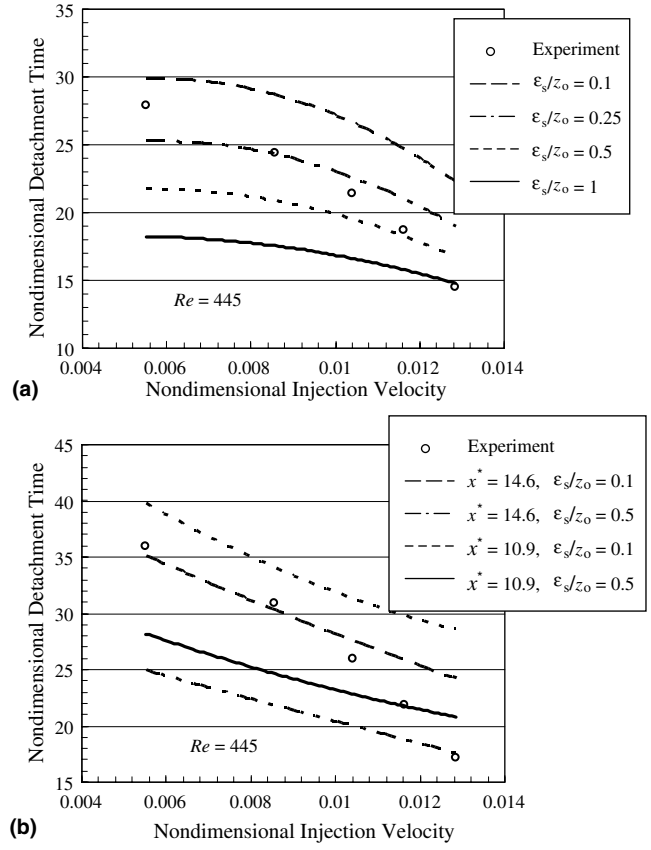

Fig. 9. Numerical and experimental data for the variation of the non-dimensional detachment time with the non-dimensional injection velocity carried out for several normalized initial perturbation amplitudes ε_s/z_0 at $Re = 445$: (a) horizontal bounding surfaces ($\theta = 0°$) and (b) inclined bounding surfaces ($\theta = 2.5°$).

bation amplitude $\varepsilon_s/z_0 = 0.1$, the droplet detachment time increases by nearly 18% when using the liquid film thickness at 30 mm as compared to the thickness value at 40 mm. Additionally, similar to the case with horizontal surfaces, for high injection velocities the numerical and experimental results closely agree at higher normalized initial perturbation amplitudes ε_s/z_0 (e.g., run #W2125), while good agreement is obtained at lower ε_s/z_0 values for lower values of the injection velocity (e.g., run #W0925).

5.3. Equivalent droplet diameter

Tables 3–5 list the experimental mean (D) and standard deviation (σ) of the equivalent droplet diameter, and the corresponding numerically-predicted values, for horizontal and inclined surfaces with different injection velocities and working fluids. Based on these tables, the numerical model predictions of the equivalent droplet diameters are within two standard deviations (2σ) of the experimentally measured mean droplet diameter. Plots of the reduced equivalent droplet diameter as a function of the dimensionless injection velocity are shown in Fig. 10; the variables were scaled using the parameters given in Table 1.

Droplets detaching from horizontal liquid films have slightly larger equivalent diameter than those pinching off from inclined films. For a given injection velocity, an inclination angle of 2.5° reduces the measured mean equivalent diameter by approximately 5–8% (runs #W0925 and G0925). Although the thickness of the advected liquid films increases along the length of the inclined surfaces, droplets pinch off at axial locations corresponding to mean film thickness values smaller than those values measured for the horizontal liquid films with the same injection velocity ($h_0 = 614.4$ and 686.2 μm for #W090 and #G090, respectively). Thus, the volume of liquid feeding the detached droplets for horizontal surfaces is greater than the volume available at the detachment axial location for droplets pinching off from inclined surfaces.

An atomization mechanistic model for the size of detached droplets based on a balance between gravitational and surface tension forces provides a theoretical estimate for the droplet diameter for the case of zero injection velocity [37]

$$D_{\text{theory}} = 3.3\left(\frac{\sigma}{\rho g}\right)^{0.5} \tag{7}$$

The corresponding values for water and 20% glycerol at 293 K are 9.0 and 8.7 mm, respectively; these values agree reasonably well with the experimental data for the case with injection. The data obtained here indicate that the equivalent droplet diameter increases with injection velocity; this trend can be attributed to the development of thicker liquid films when higher injection velocities are used.

5.4. Penetration depth of spikes

The penetration depth is defined as the maximum vertical distance from the horizontal plate surface to the lower tip of the developing spike immediately prior to droplet detachment. Tables 3–5 include values for the experimental mean (d) and standard deviation (σ) for the maximum penetration depth for horizontal and inclined surfaces with both working fluids at different injection velocities; numerically predicted values for the maximum penetration depth are also given. Based on these data, it is clear that the maximum penetration depth increases when the injection velocity increases or when 20% glycerol is used as a working fluid instead of water. An increase of nearly 72% in the experimental mean value of the maximum penetration depth is obtained when the injection velocity increases from 0.9 to 2.1 mm/s using water ($\theta = 0°$). At higher injection velocities, the thickness (h_0) of the liquid film increases providing more liquid to the developing spikes (e.g., $h_0 = 0.614$ and 1.506 mm for #W090 and #W210, respectively). Plots of the reduced maximum penetration depth as a function of the dimensionless injection velocity are shown in Fig. 11; the variables were scaled using the parameters given in Table 1.

The horizontal liquid films have higher penetration depths than the inclined films for the same transpiration

Table 4
Experimental mean, standard deviation (σ) and numerical prediction values of the detachment time (t_d), equivalent droplet diameter (D) and maximum penetration depth (d) for the experimental and numerical runs conducted using inclined bounding surfaces ($\theta = 2.5°$) and the corresponding liquid film thickness at $x_2 = 30$ mm and $x_3 = 40$ mm for water at 293 K

Runs	Experiment		Normalized initial perturbation amplitude, ε_s/z_0				
			0.1	0.25	0.5	0.75	1
	t_d (s)	σ (s)	*Numerical predictions $t_d\|x_2$ (s)/$t_d\|x_3$ (s)*				
W0925	0.5991	0.0114	0.6657	0.5541	0.4717	0.4232	0.3876
			0.5874	0.4902	0.4171	0.3774	0.3477
W1425	0.5155	0.0098	0.5582	0.4701	0.4041	0.3671	0.3407
			0.4986	0.4186	0.3599	0.3262	0.3032
W1725	0.4322	0.0094	0.5328	0.4498	0.3879	0.3519	0.3277
			0.4658	0.3912	0.3378	0.3068	0.2853
W1925	0.3641	0.0129	0.4989	0.4221	0.3638	0.3298	0.3074
			0.4341	0.3657	0.3147	0.2866	0.2688
W2125	0.2867	0.0108	0.4726	0.4002	0.3444	0.3128	0.2927
			0.4009	0.3387	0.2922	0.2695	0.2545
	D (mm)	σ (mm)	*Numerical predictions $D\|x_2$ (mm)/$D\|x_3$ (mm)*				
W0925	7.79	0.15	7.78	7.80	7.89	7.88	7.99
			7.86	7.87	7.96	7.97	8.05
W1425	8.29	0.14	8.18	8.15	8.16	8.17	8.22
			8.37	8.36	8.41	8.46	8.54
W1725	8.69	0.10	8.34	8.30	8.33	8.35	8.40
			8.58	8.61	8.63	8.72	8.82
W1925	9.01	0.13	8.48	8.37	8.49	8.56	8.59
			8.77	8.79	8.91	9.01	9.08
W2125	9.24	0.14	8.67	8.59	8.66	8.72	8.74
			8.99	9.06	9.21	9.33	9.49
	d (mm)	σ (mm)	*Numerical predictions $d\|x_2$ (mm)/$d\|x_3$ (mm)*				
W0925	44.34	2.33	41.57	40.34	40.45	41.35	41.36
			42.44	42.43	43.29	46.17	47.35
W1425	54.08	2.39	47.66	47.47	48.34	50.42	52.06
			51.92	52.58	54.65	56.79	58.97
W1725	61.84	1.76	52.08	51.75	52.39	53.61	55.62
			57.92	58.06	61.01	63.19	65.33
W1925	70.72	2.25	54.92	55.76	56.78	57.89	60.07
			62.47	63.23	65.29	68.63	72.61
W2125	80.72	2.66	58.75	60.05	60.46	62.12	65.34
			69.46	70.40	72.80	77.86	82.22

Table 5
Experimental mean, standard deviation (σ) and numerical prediction values of the detachment time (t_d), equivalent droplet diameter (D) and maximum penetration depth (d) for the experimental and numerical runs conducted using inclined surfaces ($\theta = 2.5°$) and the corresponding liquid film thickness at $x_1 = 20$ mm and $x_2 = 30$ mm for 20% glycerol at 293 K

Runs	Experiment		Normalized initial perturbation amplitude, ε_s/z_0				
			0.05	0.25	0.5	0.75	1
	t_d (s)	σ (s)	*Numerical predictions $t_d\|x_1$ (s)/$t_d\|x_2$ (s)*				
G0925	0.8122	0.0127	0.8428	0.6516	0.5605	0.4987	0.4554
			0.7984	0.5794	0.4860	0.4351	0.3991
G1725	0.6449	0.0164	0.6781	0.5201	0.4472	0.4051	0.3754
			0.6236	0.4774	0.4110	0.3714	0.3452
	D (mm)	σ (m)	*Numerical predictions $D\|x_1$ (mm)/$D\|x_2$ (mm)*				
G0925	8.25	0.17	7.80	7.91	7.80	7.82	7.76
			8.12	7.89	7.90	7.89	7.96
G1725	8.98	0.21	8.60	8.30	8.26	8.26	8.28
			8.64	8.42	8.39	8.44	8.49
	d (mm)	σ (mm)	*Numerical predictions $d\|x_1$ (mm)/$d\|x_2$ (mm)*				
G0925	54.37	2.87	54.88	44.47	45.37	44.33	45.41
			52.21	47.53	46.33	47.43	48.52
G1725	68.8	2.84	60.94	56.59	55.91	56.95	58.05
			60.69	61.25	62.18	63.04	65.29

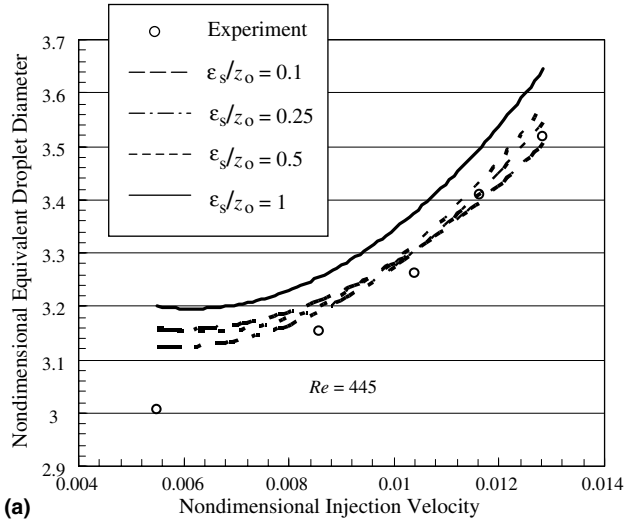

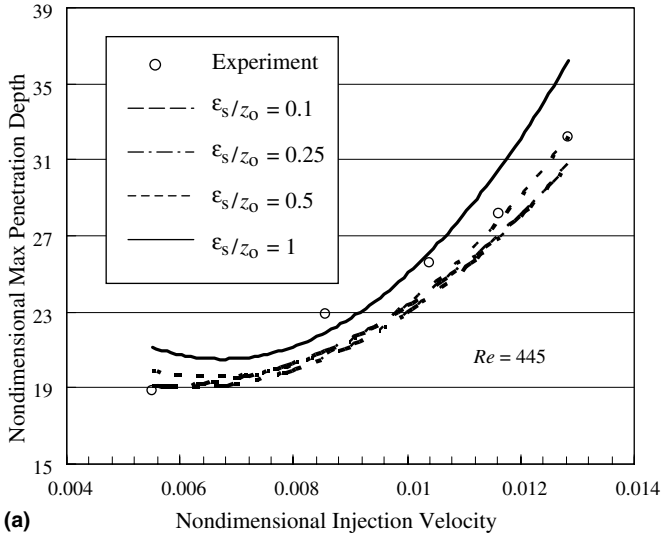

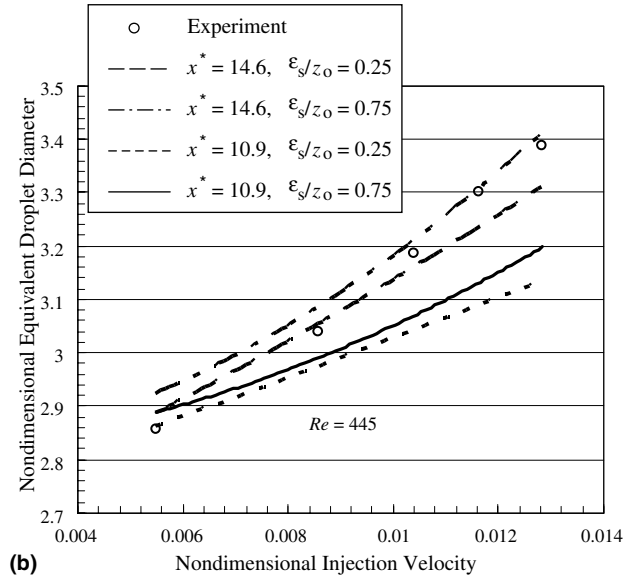

Fig. 10. Numerical and experimental data for the variation of the non-dimensional equivalent droplet diameter with the non-dimensional injection velocity carried out for several normalized initial perturbation amplitudes ε_s/z_0 at $Re = 445$: (a) horizontal bounding surfaces ($\theta = 0°$) and (b) inclined bounding surfaces ($\theta = 2.5°$).

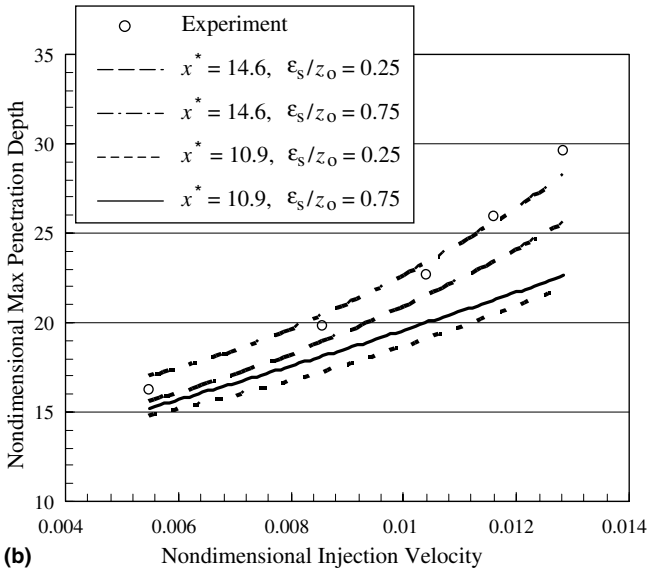

Fig. 11. Numerical and experimental data for the variation of the non-dimensional maximum penetration depth with the non-dimensional injection velocity carried out for several normalized initial perturbation amplitudes ε_s/z_0 at $Re = 445$: (a) horizontal bounding surfaces ($\theta = 0°$) and (b) inclined bounding surfaces ($\theta = 2.5°$).

velocity and working fluid. The mean liquid film thickness value for horizontal films is, however, higher than the local liquid thickness value at which droplets detach in the axial direction of inclined liquid films as given in Table 2. This can be attributed to the tangential flow component for the inclined liquid films.

The time history of the penetration depth is investigated and traced for both horizontal and inclined liquid films. Figs. 12 and 13 show transient variations in the experimental and numerical non-dimensional penetration depths. The numerical simulations were conducted using different values of the normalized initial perturbation amplitude, while employing the liquid film thickness at specific axial locations for the inclined films. In all cases, the numerical predicts are qualitatively similar to the experimental data. The end points on these graphs correspond to droplet detachments; clearly, for thick liquid films (i.e., higher w_{in}) better agreement between the numerical and experimental results is obtained at higher normalized perturbation amplitudes, while the opposite is true for thin liquid films (i.e., lower w_{in}). The initial perturbation geometry used in the numerical simulations (saddle type perturbation, Eq. (6)) is highly idealized and is unlikely to be exactly duplicated in the experiments. For experiments with high injection velocities, the film quickly thickens and a large perturbation approximating that used in the numerical simulations is formed.

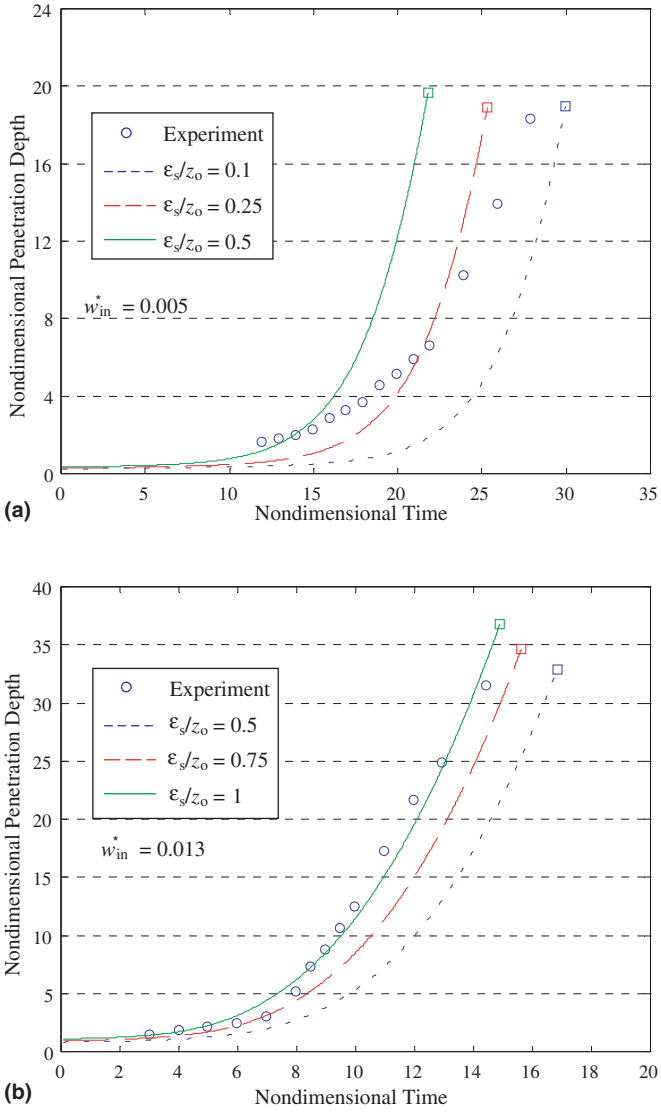

Fig. 12. Numerical and experimental data for the transient variation of the non-dimensional penetration depth carried out for horizontal surfaces ($Re = 445$, $\theta = 0°$): (a) $w^*_{in} = 0.005$ and (b) $w^*_{in} = 0.013$.

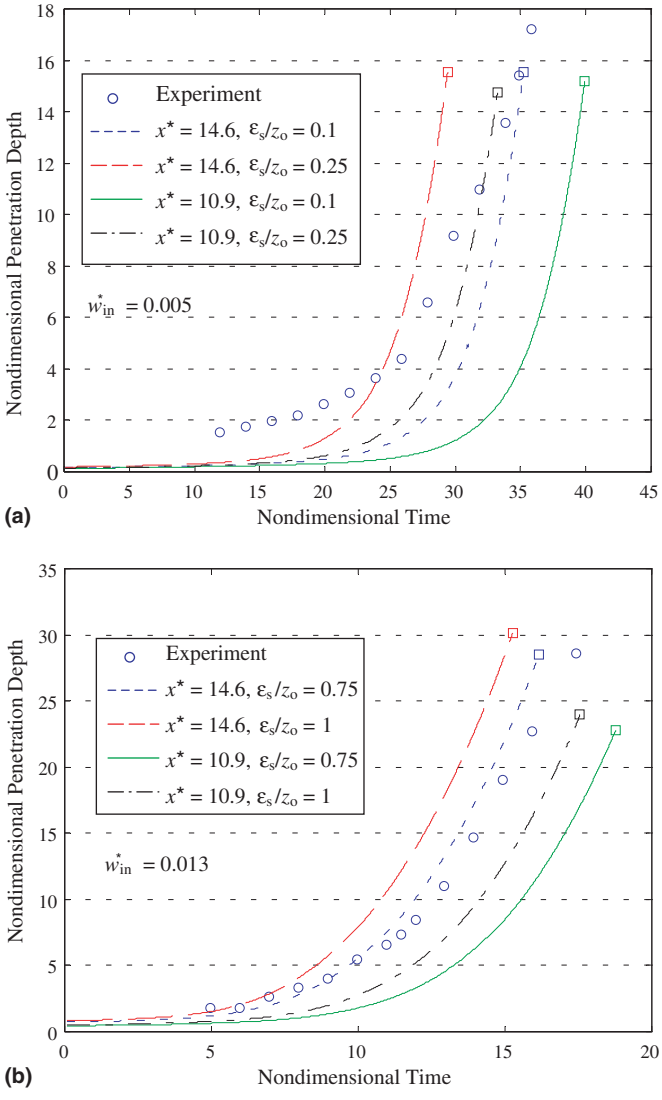

Fig. 13. Numerical and experimental data for the transient variation of the non-dimensional penetration depth carried out for inclined surfaces ($Re = 445$, $\theta = 2.5$): (a) $w^*_{in} = 0.005$ and (b) $w^*_{in} = 0.013$.

However, for low injection velocities, small random surface perturbations interact during the time of film growth, so that the surface geometry may be significantly different from that assumed in the simulations. These differences in initial perturbation geometry may be the reason for the qualitatively different penetration depth behavior observed in the early part of the disturbance for low and high injection velocities (Figs. 12(a) and 13(a) vs. 12(b) and 13(b)).

6. Concluding remarks

An experimental and numerical investigation has been carried out to analyze the Rayleigh–Taylor instability for bounded liquid films with injection through the boundary. Different aspects of the liquid film morphology and evolution have been examined, including evolution of liquid film thickness, droplet detachment time, equivalent size for detached droplets, and penetration depth for bounded liquid films.

The liquid film injection velocity through the bounding surface affects several flow parameters. A higher injection velocity through the boundary increases the unperturbed liquid film thickness; the equivalent droplet diameter of the detaching droplets and the maximum penetration depth of the developing spikes also increase because of the corresponding increase in the liquid volume at higher injection velocities. The detachment time increases by decreasing the injection velocity due to the development of thinner liquid films. Water and water–glycerol solution (20 wt%) are used as working fluids to extend the fluid parameters and the range of comparison between the experiments and the numerical front tracking model. Experiments using

glycerol solution have thicker unperturbed liquid films than the corresponding water runs at the same injection velocity w_{in}, and hence larger equivalent droplet diameter and maximum penetration depth.

Inclined (vs. horizontal) bounding surfaces provide a different behavior for the liquid film. The thickness of the advected liquid film increases along the axial direction of the bounding surface due to the continuous injection and delayed droplet formation as a result of the tangential acceleration and associated shear stress, and the liquid film drift. Droplets detaching from horizontal liquid films have larger equivalent diameters and penetration depths than those pinching off from inclined films. In inclined liquid films, droplets detach at axial locations corresponding to mean liquid film thickness values that are smaller than those measured for horizontal liquid films at a given injection velocity.

Good agreement has generally been obtained between the experimental data and predictions of a numerical model based on the level contour front tracking method. The model can be used to identify parameter ranges for successful operation of the wetted wall protection concept.

Acknowledgements

This work was performed in support of the ARIES-IFE project. Numerous discussions with members of the ARIES project team are gratefully acknowledged. Financial support was provided in part by the US Department of Energy through contract # DE-FG02-01ER54656.

References

[1] S. Chandrasekhar, Hydrodynamic and Hydromagnetic Stability, Clarendon, 1961.
[2] Y.-N. Young, H. Tufo, A. Dubey, R. Rosner, On the miscible Rayleigh–Taylor instability: two and three dimensions, J. Fluid Mech. 447 (2001) 377–408.
[3] L.A. Booth (Compiler), Central station power generation by laser-driven fusion, LA-4858-MS, Los Alamos Scientific Laboratory Report, 1972.
[4] J.M. Williams et al., A conceptual laser controlled thermonuclear reactor power plant, in: Proceedings First Topical Meeting Technology of Controlled Fusion, San Diego, CA, 1974.
[5] L.M. Waganer et al., Inertial fusion energy reactor design studies, McDonnell Douglas Report, DOE/ER-4101, MDC 92E0008, vol. III, March 1992.
[6] M.A. Abdou et al., Critical technical issues and evaluation and comparison studies for inertial fusion energy reactors, Fus. Eng. Des. 23 (1993) 251–297.
[7] Osirus and Sombrero Inertial Fusion Power Plant Designs, Final Report, WJSA-9201, DOE/ER/54100-1, March 1992.
[8] HIBALL—A conceptual heavy ion beam driven fusion reactor study preliminary report, University of Wisconsin Report, UWFDM -450, June 1981.
[9] J.E. Eggleston, M.A. Abdou, M.S. Tillack, Analysis of the energy transport and deposition within the reaction chamber of the Prometheus inertial fusion energy reactor, Fus. Eng. Des. 27 (1995) 226–231.
[10] N.B. Morley, Geometric and blast effects on thin film cavity protection schemes for IFE reactors, in: Proceedings of the 16th IEEE/NPSS Symposium on Fusion Energy, Champaign, Urbana IL, October 1995.
[11] S. Shin, A level contour reconstruction method for three-dimensional multiphase flows and its application, Ph.D. Thesis, Georgia Institute of Technology, 2002.
[12] S. Shin, F. Abdelall, D. Juric, S.I. Abdel-Khalik, M. Yoda, D. Sadowskiand the ARIES Team, Fluid dynamic aspects of the porous wetted wall protection scheme for inertial fusion energy reactors, Fus. Sci. Technol. 43 (2003) 366–377.
[13] F.F. Abdelall, Experimental and numerical studies of the Rayleigh–Taylor instability for bounded liquid films with injection through the boundary, Ph.D. Thesis, Georgia Institute of Technology, 2004.
[14] S. Shin, D. Juric, Modeling three-dimensional multiphase flow using a level contour reconstruction method for front tracking without connectivity, J. Comput. Phys. 180 (2002) 427–470.
[15] D.H. Sharp, An overview of Rayleigh–Taylor instability, Physica D 12 (1984) 3–18.
[16] S.G. Yiantsios, B.G. Higgins, Rayleigh–Taylor instability in thin viscous films, Phys. Fluids A 1 (1989) 1484–1501.
[17] L.A. Newhouse, C. Pozrikidis, The Rayleigh–Taylor instability of a viscous liquid layer resting on a plane wall, J. Fluid Mech. 217 (1990) 615–638.
[18] D.J. Lewis, The instability of liquid surfaces when accelerated in a direction perpendicular to their planes. II, Proc. R. Soc. London Ser. A 202 (1950) 81–96.
[19] R.E. Duff, F.H. Harlow, C.W. Hirt, Effects of diffusion on interface instability between gases, Phys. Fluids 5 (1962) 417–425.
[20] R. Popil, F.L. Curzon, Production of reproducible Rayleigh–Taylor instabilities, Rev. Sci. Instrum. 50 (1979) 1291–1295.
[21] A. Lange, M. Schröter, M.A. Scherer, A. Engel, I. Rehberg, Fingering instability in a water–sand mixture, Eur. Phys. J. B 4 (1998) 475–484.
[22] S.G. Bankoff, Minimum thickness of a draining liquid film, Int. J. Heat Mass Transfer 14 (1971) 2143–2146.
[23] S.G. Bankoff, S.H. Davis, Stability of thin films, PhysChem. Hydrodyn. 9 (1987) 5–7.
[24] B.D. Nichols, C.W. Hirt, R.S. Hotchkiss, SOLA-VOF: A solution algorithm for transient fluid flow with multiple free boundaries, Technical Report LA-8355, Los Alamos Scientific Laboratory, 1980.
[25] J. Glimm, O. Mcbryan, R. Menikoff, D.H. Sharp, Front tracking applied to Rayleigh–Taylor instability, SIAM J. Sci. Stat. Comput. 7 (1986) 230–251.
[26] J. Zhu, J.A. Sethian, Projection methods coupled to level set interface techniques, J. Comput. Phys. 102 (1992) 128.
[27] S. Chen, G.D. Doolen, Lattice Boltzmann method for fluid flows, Ann. Rev. Fluid Mech. 30 (1998) 329.
[28] G. Tryggvason, S.O. Unverdi, Computations of three-dimensional Rayleigh–Taylor instability, Phys. Fluids A 2 (1990) 656–659.
[29] S.O. Unverdi, G. Tryggvason, A front-tracking method for viscous, incompressible, multi-fluid flows, J. Comput. Phys. 100 (1992) 25–37.
[30] G. Tryggvason, B. Bunner, A. Esmaeeli, D. Juric, N. Al-Rawahi, W. Tauber, J. Han, S. Nas, Y.J. Jan, A front tracking method for the computations of multiphase flow, J. Comput. Phys. 169 (2001) 708–759.
[31] X.L. Li, Study of three-dimensional Rayleigh–Taylor instability in compressible fluids through level set method and parallel computation, Phys. Fluids A 5 (1993) 1904–1913.
[32] G.I. Taylor, The instability of liquid surfaces when accelerated in a direction perpendicular to their planes. I, Proc. R. Soc. London Ser. A 201 (1950) 192–196.
[33] X. He, R. Zhang, S. Chen, G.D. Doolen, On the three-dimensional Rayleigh–Taylor instability, Phys. Fluids 11 (1999) 1143–1152.
[34] J.W. Cooke, S. Cantor, Physical properties of molten-salt reactor coolant and flush salts, Oak Ridge National Laboratory, TM 2316, 1968.

[35] K. Furukawa, H. Ohno, Molten materials I: molten LiF–BeF_2 (flibe) system, The Society of Molten-Salt Thermal Technology, Japan Nuclear Energy Information Center, 1980.
[36] P. Gierszewski, B. Mikic, N. Todreas, Property calculation for lithium, sodium, helium, flibe and water in fusion reactor applications, Research Report PFC-RR-80-12, Fusion Blanket and Structures Group, Plasma Fusion Center, Massachusetts Institute of Technology, 1980.
[37] C.E. Lapple, J.P. Henry, D.E. Blake, Atomization—a survey and critique of the literature, Research Report DA-18-035-AMC-122(A), SRI No. 6, Stanford Research Institute, 1967.